ChemPubSoc Europe

DOI: 10.1002/cssc.201801962

CHEMSUSCHEM Full Papers

# A Water-Soluble NaCMC/NaPAA Binder for Exceptional Improvement of Sodium-Ion Batteries with an $SnO_2$-Ordered Mesoporous Carbon Anode

Jagabandhu Patra,[a, b, f] Purna Chandra Rath,[a, b] Chi Li,[a] Hsien-Ming Kao,[c] Fu-Ming Wang,[d] Ju Li,*[e] and Jeng-Kuei Chang*[a, b, e, f]

$SnO_2$@CMK-8 composite, a highly promising anode for Na-ion batteries (NIBs), was incorporated with polyvinylidene difluoride (PVDF), sodium carboxymethylcellulose (NaCMC), sodium polyacrylate (NaPAA), and NaCMC/NaPAA mixed binders to optimize the electrode sodiation/desodiation properties. Synergistic effects between NaCMC and NaPAA led to the formation of an effective protective film on the electrode. This coating layer not only increased the charge–discharge Coulombic efficiency, suppressing the accumulation of solid–electrolyte interphases, but also kept the $SnO_2$ nanoparticles in the CMK-8 matrix, preventing the agglomeration and removal of oxide upon cycling. The adhesion strength and stability towards the electrolyte of the binders were evaluated. In addition, the charge–transfer resistance and apparent $Na^+$ diffusion of the $SnO_2$@CMK-8 electrodes with various binders were examined and post-mortem analyses were conducted. With NaCMC/NaPAA binder, exceptional electrode capacities of 850 and 425 mAh $g^{-1}$ were obtained at charge–discharge rates of 20 and 2000 mA $g^{-1}$, respectively. After 300 cycles, 90% capacity retention was achieved. The thermal reactivity of the sodiated electrodes was studied by using differential scanning calorimetry. The binder effects on NIB safety, in terms of thermal runaway, are discussed.

## Introduction

Rechargeable Na-ion batteries (NIBs) are an appealing alternative or complementary technology to lithium-ion batteries (LIBs) for large-scale energy storage.[1,2] The main incentive for using NIBs is the abundance, global distribution, and low cost of sodium precursors.[3] However, NIBs are still in the early stages of development. For example, although there has been decent progress on cathode materials, including layered oxides, polyanionic compounds, Prussian blue analogues, and organic compounds,[4–8] finding a good anode is relatively challenging because the commonly used LIB graphite anode has poor $Na^+$ storage capability.[9,10] In addition to electrode materials, there are many components in NIBs, such as binders, conductive agents, electrolytes, additives, and separators.[11–15] These seemingly minor parts significantly affect the performance of NIBs.[16]

In general, the main function of polymer binders is to glue the active materials and conductive agents to the current collector, to maintain mechanical integrity, simultaneous electronic and ionic percolation, and to reduce thickness expansion. The importance of binders is usually overlooked, as they account for only approximately 5 wt% of the electrode material and directly contribute little to the capacity.[11,17,18] Polyvinylidene difluoride (PVDF) is a widely used binder in LIBs owing to its acceptable bonding capability and electrochemical stability.[19] PVDF is usually dissolved in volatile, flammable, and toxic *N*-methyl pyrrolidone (NMP) solvent for electrode slurry preparation, which requires special care of the processing conditions, and thus has a high production cost.[18,20] Moreover, both PVDF and NMP are expensive and difficult to recycle. For NIB applications, it has been reported that PVDF tends to defluorinate during sodiation, leading to loss of electrode integrity.[21] In this context, new water-soluble binders have recently at-

[a] Dr. J. Patra, Dr. P. C. Rath, C. Li, Prof. J.-K. Chang
Institute of Materials Science and Engineering
National Central University
300, Zhongda Road, Taoyuan, 320 (Taiwan)
E-mail: jkchang@nctu.edu.tw

[b] Dr. J. Patra, Dr. P. C. Rath, Prof. J.-K. Chang
Department of Materials Science and Engineering
National Chiao Tung University
1001, University Road, Hsinchu, 300 (Taiwan)

[c] Prof. H.-M. Kao
Department of Chemistry
National Central University
300, Zhongda Road, Taoyuan, 320 (Taiwan)

[d] Prof. F.-M. Wang
Graduate Institute of Applied Science and Technology
National Taiwan University of Science and Technology
43, Keelung Road, Taipei, 106 (Taiwan)

[e] Prof. J. Li, Prof. J.-K. Chang
Department of Nuclear Science and Engineering and Department of Materials Science and Engineering
Massachusetts Institute of Technology
77 Massachusetts Avenue, Cambridge, MA 02139 (USA)
E-mail: liju@mit.edu

[f] Dr. J. Patra, Prof. J.-K. Chang
Hierarchical Green-Energy Materials (Hi-GEM) Research Centre
National Cheng Kung University, 1, University Road, Tainan, 701 (Taiwan)

Supporting information and the ORCID identification number(s) for the author(s) of this article can be found under: https://doi.org/10.1002/cssc.201801962.

tracted a lot of attention for LIBs and NIBs owing to their low cost, nontoxicity, short drying time, easy processing, and great bonding ability.[22–26] Cost-effectiveness and large-scale applications are emphasized for NIBs. Therefore, the use of appropriate and inexpensive binders to improve battery performance is more desirable than developing sophisticated active materials for the same purpose. The radius of $Na^+$ (1.02 Å) is larger than that of $Li^+$ (0.76 Å); therefore, the electrode volume variation upon charging/discharging of NIBs is higher than that of LIBs.[27] This implies that binders can play a more significant role in determining performance for NIBs. All these factors justify the importance of further study of water-soluble binders for NIBs.

$SnO_2$ has attracted much attention as an NIB anode because it is chemically stable, readily available, nontoxic, and has a high theoretical capacity.[28–31] Recently, we proposed a unique three-dimensional (3D) architectured $SnO_2$@CMK-8 electrode with a high tap density.[32] CMK stands for "carbon mesostructured by KAIST", to mark the contribution from KAIST, Korea, for template-assisted fabrications of mesoporous carbons.[33] CMK-8 is a kind of 3D mesoporous carbon with an *Ia3d* symmetry, which can be prepared by using ordered porous silica KIT-6 as a hard template for nanocasting.[34] With optimized electronic and ionic conduction in the electrode, $SnO_2$ nanoparticles (NPs) underwent a conversion reaction ($SnO_2 + 4Na^+ + 4e^- \leftrightarrow Sn + Na_2O$) and then an alloying reaction ($Sn + 3.75Na^+ + 3.75e^- \leftrightarrow {}^1/_4 Na_{15}Sn_4$), resulting in a reversible capacity of as high as 800 mAh $g^{-1}$.[32] This electrode is quite promising, even though PVDF binder was used. However, there are some issues (e.g., relatively low (ca. 55%) first-cycle Coulombic efficiency (CE), limited rate capability, and nonideal cycling stability) that must be overcome before practical applications become feasible. The effects of binder selection on the electrochemical performance of a $SnO_2$-based NIB anode are still unclear; various binders have been arbitrarily chosen in previous studies (PVDF is the most common).[35–37] The only study on binders for $SnO_2$ anodes showed that polyacrylic acid (PAA)-soluble starch (SS) binder was superior to the conventional PDVF binder in terms of electrode durability.[38] However, the $SnO_2$ capacity was relatively low (i.e., 370 mAh $g^{-1}$@100 mA $g^{-1}$), so the volume expansion/shrinkage during cycling was relatively gentle (less harsh on binders). A more systematic and detailed investigation is needed.

Binder selection can be electrode-material-specific. Komaba et al. found that a hard carbon anode with sodium carboxymethyl cellulose (NaCMC) binder has better reversibility and cyclability than those of an electrode with PVDF binder.[21] With NaCMC binder, the hard carbon derived from cherry petals showed a high initial capacity of 310 mAh $g^{-1}$ and great cycling stability.[39] NaCMC binder was also found to improve the CE, rate capability, and stability of a $Na_2Ti_6O_{13}$ anode.[40] It was recently reported that a $Na_3V_2(PO_4)_2F_3$ cathode with NaCMC binder has excellent high-rate performance and cycle life (i.e., 75 mAh $g^{-1}$@70 C and 79% capacity retention after 3500 cycles).[24] In addition, NaCMC binder was found to be also suitable for phosphorus/carbon nanotube (CNT), $PbTiO_3$, and $Na_{0.44}MnO_2$ electrodes.[25,41,42] However, opposite results have also been reported; for example, a sodium Prussian blue/PVDF electrode showed superior charge–discharge performance to that prepared with NaCMC binder.[43] Contradictory results have also been reported for sodium polyacrylate (NaPAA) binder, which can outperform PAA binder owing to its more favorable polymer conformation and because $Na^+$ can improve the solid–electrolyte interphase (SEI) properties.[23,44] N-doped CNT[45] and $FeS_2$[26] anodes with NaPAA binder exhibited excellent capacity, CE, and cycling stability, whereas an Sn-Co anode with the same binder showed poor durability.[46] Therefore, an appropriate binder must be selected for a given electrode material to optimize electrochemical performance. The development of a good binder for high-capacity $SnO_2$ anodes of NIBs is the goal of the present work.

The thermochemical stability of sodiated anodes is a crucial property that affects thermal runaway in practical NIBs. Two key factors are of major concern: (i) the exothermic onset temperature, which governs the initial step that triggers a fire/explosion, and (ii) the total heat released, which is indicative of the magnitude of reaction enthalpy.[47,48] Both factors are associated with the thermal stability of the SEI layer.[47,48] Because the binder can affect SEI chemistry,[49] it is expected that the electrode thermal reactivity will vary with binder type. However, this topic has received little attention to date. In this study, we investigated this issue for NIBs by using differential scanning calorimetry (DSC). PVDF, NaCMC, NaPAA, and mixed NaCMC/NaPAA binders were systematically compared in terms of crystallinity, bonding strength, stability, the resulting electrode morphology, surface chemistry, impedance, and sodiation/desodiation properties.

## Results and discussion

Figure 1a shows the wide-angle XRD pattern of the $SnO_2$@CMK-8 sample. All peaks were attributed to various crystallographic planes of standard tetragonal $SnO_2$ (JCPDS 41-1445). The crystallinity of CMK-8 was too low to exhibit distinct diffraction signals. The broad peaks indicated that $SnO_2$ had a small crystal size. The microstructure of $SnO_2$@CMK-8 examined by TEM is shown in Figure 1b. The $SnO_2$ NPs (dark spots), with a uniform size of approximately 2(±1) nm, were highly dispersed and well-confined within the 3D porous CMK-8 matrix (bright framework). The $SnO_2$/CMK-8 weight ratio was approxi-

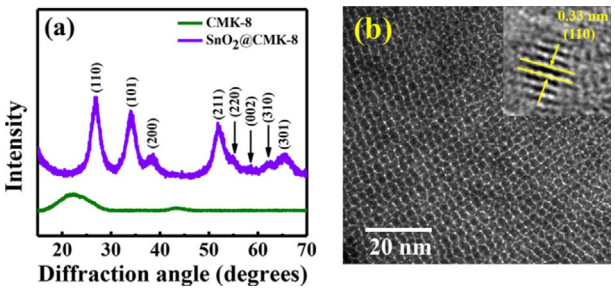


**Figure 1.** (a) Wide-angle XRD pattern and (b) TEM images of the $SnO_2$@CMK-8 composite.

mately 85:15.[32] The small-angle XRD data for pristine CMK-8 and $SnO_2$@CMK-8 samples are shown in Figure S2 (see the Supporting Information). The intensities of the 1.1° and 1.3° peaks, which corresponded to (211) and (220) superlattice diffractions, respectively, of the CMK-8 highly ordered mesoporous structure with an *Ia3d* symmetry,[50] significantly decreased after $SnO_2$ incorporation. This confirmed that most of the mesopores of CMK-8 were filled with $SnO_2$ NPs.

The thermal stability of the binders was evaluated by TGA; the obtained data are shown in Figure S3. Considering the hydrophilicity of NaCMC and NaPAA, the gradual weight loss before approximately 150 °C for the two binders was attributed to the removal of absorbed water. NaCMC showed the lowest decomposition temperature (ca. 300 °C), producing $Na_2O$ and $Na_2CO_3$.[51] PVDF decomposed at approximately 420 °C with a huge weight drop of >60%. NaPAA had the highest thermal stability (i.e., the smallest weight loss, 25%, at the highest temperature, 460 °C). For any binder, the decomposition temperature was much higher than that used for slurry drying (i.e., ca. 100 °C); therefore, binder thermal stability was not an issue during the electrode fabrication process.

The bonding ability of the binders was evaluated using peel tests. Scotch tape was adhered to the electrode and then manually peeled off to test the adhesion. As shown in Figure S4, for the PVDF sample, the active material layer was mostly removed from the substrate. With the NaCMC binder, the adhesion between Cu foil and the coating material layer was improved. However, the connection between the $SnO_2$@CMK-8 NPs was still not strong, as a clearly detached film was found on the tape side. The NaPAA binder enhanced the interparticle adhesion even more, as the amount of $SnO_2$@CMK-8 on the tape was reduced. The highest adhesion strength was found for NaCMC/NaPAA mixed binder. The carbonyl and carboxyl groups on the binders can form hydrogen bonds between the polymer chains and interact with $SnO_2$ and the current collector to maintain mechanical stability.[17,52] In addition to being an adhesive, NaCMC is also a dispersant,[11,53] which can modify the conformation of the mixed binder and increase the number of bonding sites with the active material and Cu foil, which reduces the flaw size[54] and leads to excellent adhesion of the electrode.

Figure 2a shows the initial five cyclic voltammetry (CV) curves of the $SnO_2$@CMK-8 electrode with NaCMC/NaPAA binder. In the first negative scan, there were small humps at approximately 1.5–2.0 V, which were associated with the surface group reduction at the electrode. The irreversible peak at approximately 0.8 V was attributed to the decomposition of fluoroethylene carbonate and the formation of SEI.[13,55] A conversion reaction of $SnO_2$ with $Na^+$ then occurred, which formed Sn and $Na_2O$. When the potential was scanned towards even lower voltage (<0.3 V), another cathodic peak arose, indicating the occurrence of Sn-Na alloying reactions (forming $NaSn_5$, NaSn, $Na_9Sn_4$, $Na_{15}Sn_4$).[56,57] Below 0.1 V, $Na^+$ insertion into the carbon phase can also take place.[58] In the following positive scan, the reverse reactions (i.e., deinsertion, dealloying, and reconversion) occurred, contributing to the anodic peaks. The CV redox behavior became stable in the subsequent scans.

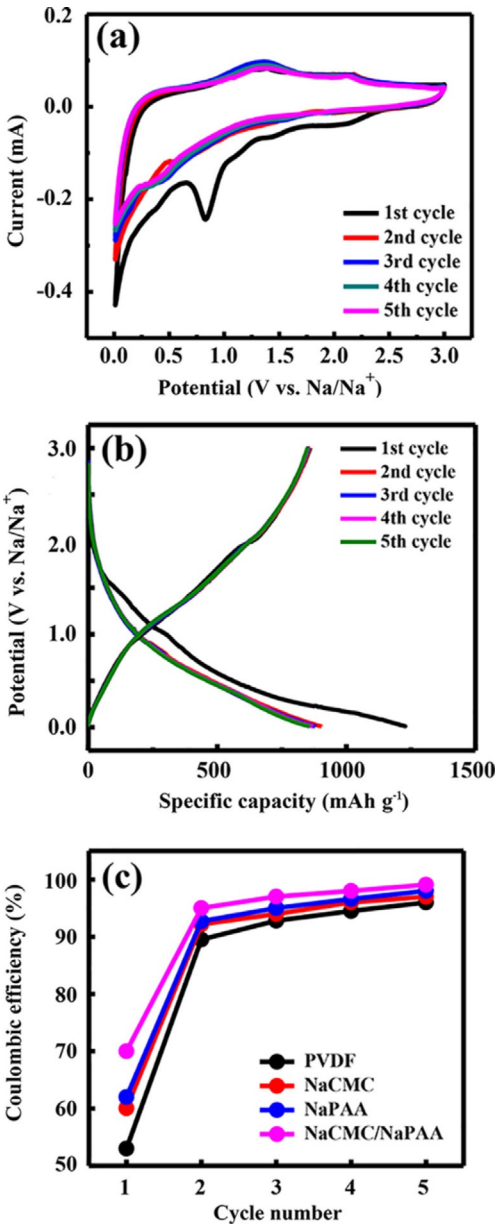


**Figure 2.** (a) CV curves of the NaCMC/NaPAA electrode measured at a scan rate of 0.1 mV $s^{-1}$. (b) Initial five charge–discharge curves of the NaCMC/NaPAA electrode measured at 20 mA $g^{-1}$. (c) The CE values versus cycle number for the electrodes with various binders.

The voltammetric characteristics of the $SnO_2$@CMK-8 electrodes with other binders were similar, as shown in Figure S5.

The charge–discharge curves of various $SnO_2$@CMK-8 electrodes (for the initial five cycles) are shown in Figure 2b and Figure S6. The Coulombic inefficiency (CI ≡ 1 − CE) was ascribed to the partial trapping of Na in $SnO_2$ and the formation of an SEI layer (i.e., electrolyte decomposition).[28,30] Figure 2c indicates that the first-cycle CE values for the PVDF, NaCMC, NaPAA, and NaCMC/NaPAA electrodes were 53%, 60%, 62%, and 70%, respectively (Table 1). The initial efficiency of 70% is among the best reported (the mechanism is discussed later), with efficiencies of 30–45% common for various $SnO_2$-based NIB anodes.[30,38,55,59,60] At the fifth cycle, a CE of 99.3% was ob-

**Table 1.** Charge–discharge properties and film densities of $SnO_2$@CMK-8 electrodes with various binders.

| Binders | First-cycle CE [%] | Max. capacity[a] [mAh g$^{-1}$] | High rate capacity[b] [mAh g$^{-1}$] | Rate capability[c] [%] | Cycling retention[d] [%] | Film density [mg cm$^{-3}$] |
|---|---|---|---|---|---|---|
| PVDF | 53 | 795 | 325 | 41 | 78 | 0.40 |
| NaCMC | 60 | 800 | 345 | 43 | 83 | 0.47 |
| NaPAA | 62 | 810 | 365 | 45 | 85 | 0.47 |
| NaCMC/NaPAA | 70 | 850 | 425 | 50 | 90 | 0.48 |

[a] $C_{20}$; at 20 mA g$^{-1}$. [b] $C_{2000}$; at 2000 mA g$^{-1}$. [c] $C_{2000}/C_{20}$. [d] After 300 cycles.

tained for the NaCMC/NaPAA electrode at a low charge–discharge rate of 20 mA g$^{-1}$. The data suggest that an appropriate binder can accommodate the volume change and modify the surface chemistry of $SnO_2$@CMK-8, improving the reversibility of the electrode.

XPS was used to examine the surface chemical composition of the electrodes. The C 1s spectra of the as-prepared electrodes are shown in Figure 3a. The peak at approximately 284.6 eV corresponds to the binding energy of C–C and C–H bonds.[61,62] The PVDF electrode exhibited strong signals at 285.5 and 290.6 eV, which were attributed to $-CH_2-$ and $-CF_2-$ bonds, respectively.[61] For the aqueous binder electrodes, the 286.7 eV peak was associated with C–O bonding (for NaCMC), and the 288.5 eV peak was ascribed to the –COONa group (for both NaCMC and NaPAA).[21,63] Figure 3b presents the Sn 3d spectra of the electrodes, which show similar binding energies for all binders. The $3d^{5/2}$ and Sn $3d^{3/2}$ peaks located at 487.5 and 496.1 eV, respectively, confirmed that the valence of Sn was +4.[32,64] Interestingly, the normalized peak intensity for the electrodes decreased in the sequence PVDF > NaCMC > NaPAA > NaCMC/NaPAA. These results suggested that the NaCMC/NaPAA electrode was best covered by the binder layer, decreasing the signals from the underlying $SnO_2$. The co-existence of NaCMC and NaPAA led to a synergistic improvement in homogeneous wetting of the binder on the active particle surface, consistent with the adhesion testing results (Figure S4) before cycling.

Figure 3c compares the surface-exposed Sn content levels of various electrodes before and after five charge–discharge cycles. It was found that the surface Sn concentration of the PVDF electrode was considerably reduced after cycling, whereas that of the NaCMC/NaPAA electrode remained almost unchanged. Continuous electrolyte decomposition (suggested by the low CE; Figure 2c), and thus the growth of the SEI layer, was responsible for the clear decrease in the Sn ratio of the PVDF electrode. Figure 3d shows the F spectra of the cycled electrodes. The peak at approximately 687.6 eV for the PVDF electrode was associated with its $-CF_2-$ bond.[65,66] All the electrodes showed a new signal at approximately 684.1 eV after cycling, corresponding to NaF within the SEI, which originated from electrolyte decomposition.[66,67] The low NaF intensity for the NaCMC/NaPAA electrode further supported the suppressed SEI growth.

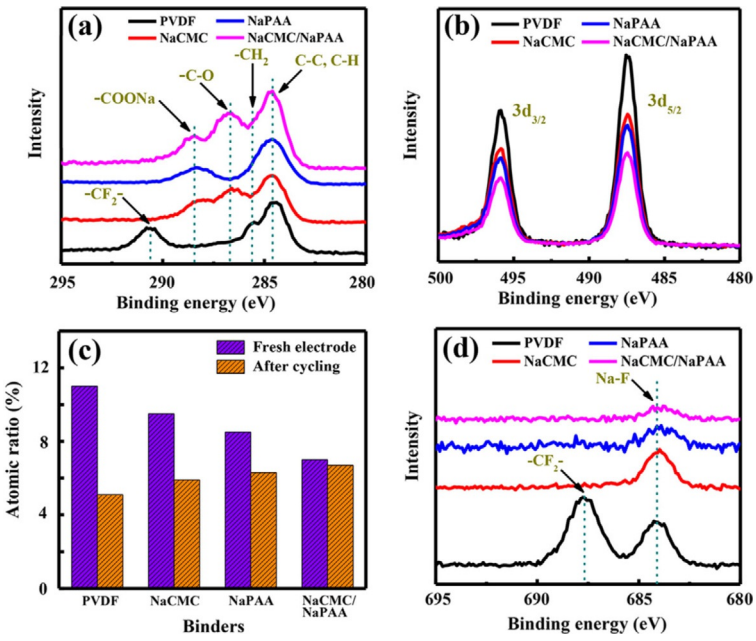


**Figure 3.** XPS (a) C 1s and (b) Sn 3d spectra of freshly prepared electrodes with various binders. (c) Comparison of Sn concentrations of various electrodes before and after five charge–discharge cycles. (d) XPS F 1s spectra of various electrodes after five charge–discharge cycles.

Figure 4 shows the electrode microstructure development. Owing to the crystalline nature (Figure S7) and bundle formation of PVDF chains,[61,62] PVDF binder cannot uniformly cover the electrode surface. The electrolyte easily permeated through PVDF and came into direct contact with the electrode material, leading to a large electrolyte decomposition reaction and high CI, especially in the first cycle. Moreover, this SEI layer did not seem to be robust enough to withstand the $SnO_2$ volume change upon charging/discharging (according to Figure 2c). The repeated breakdown and reformation of the SEI layer led to its thickening like a snow cover. In contrast, the NaCMC and NaPAA binders were fully amorphous (Figure S7) and can form a relatively continuous surface coating layer because of better wetting and spreading properties on the particle surface, which acted like an artificial SEI layer (because these binders are reasonable ionic conductors but poor electronic conductors), improving electrode passivation. In addition, this layer was mechanically stable, minimizing the growth of the SEI layer.

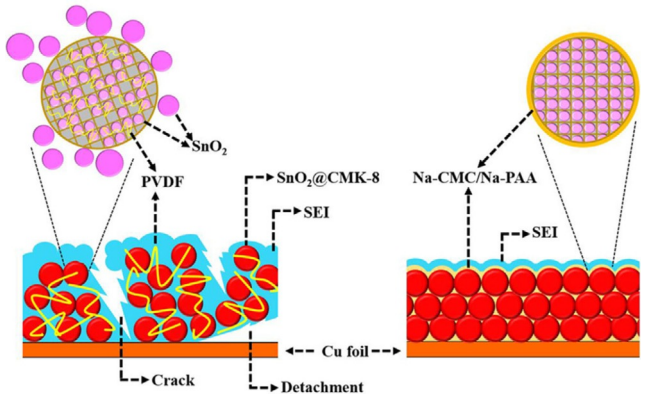


**Figure 4.** Scheme of electrode structures with PVDF and NaCMC/NaPAA binders after charge–discharge cycling.

The charge–discharge curves (after five conditioning cycles) of the $SnO_2$@CMK-8 electrodes measured at various rates are shown in Figure 5a and Figure S8. At 20 mA g$^{-1}$, the measured discharge (desodiation) capacities were 795, 800, 810, and 850 mAh g$^{-1}$ for the electrodes with PVDF, NaCMC, NaPAA, and NaCMC/NaPAA binders, respectively (Table 1). The NaCMC/NaPAA mixed binder was the most suitable for the $SnO_2$@CMK-8 electrode. With the unique 3D mesoporous architecture and appropriate selection of functional binder, the obtained electrode capacity of 850 mAh g$^{-1}$ was superior to most reported values.[30,35–38,55,59,60,64] The great bonding ability of the binder can increase the utilization of the active material. The thin SEI layer facilitated $Na^+$ transport across the electrode/electrolyte interface.[65] Moreover, the carbonyl and carboxyl groups of the binders could partially participate in the sodiation/desodiation reaction.[68] As a result, the NaCMC/NaPAA electrode had great charge–discharge capacity.

The electrode's volumetric specific capacity is also a concern for practical battery applications. The compressed densities of the PVDF, NaCMC, NaPAA, and NaCMC/NaPAA layers were 0.40, 0.47, 0.47, and 0.48 g cm$^{-3}$, respectively (including binder and carbon black; Table 1). The water-soluble binders can more closely pack the active material particles and reduce the interparticle space in the electrodes (Figure 4). The volumetric capacities of these electrodes were calculated to be 254, 301, 311, and 326 mAh cm$^{-3}$, respectively, at 20 mA g$^{-1}$. Nanostructured materials usually exhibit low volumetric performance. However, the experimental data confirm that our anode with an appropriate binder had a much higher volumetric capacity than that (130 mAh cm$^{-3}$) of a hard carbon electrode, which is the most commonly studied NIB anode.[69]

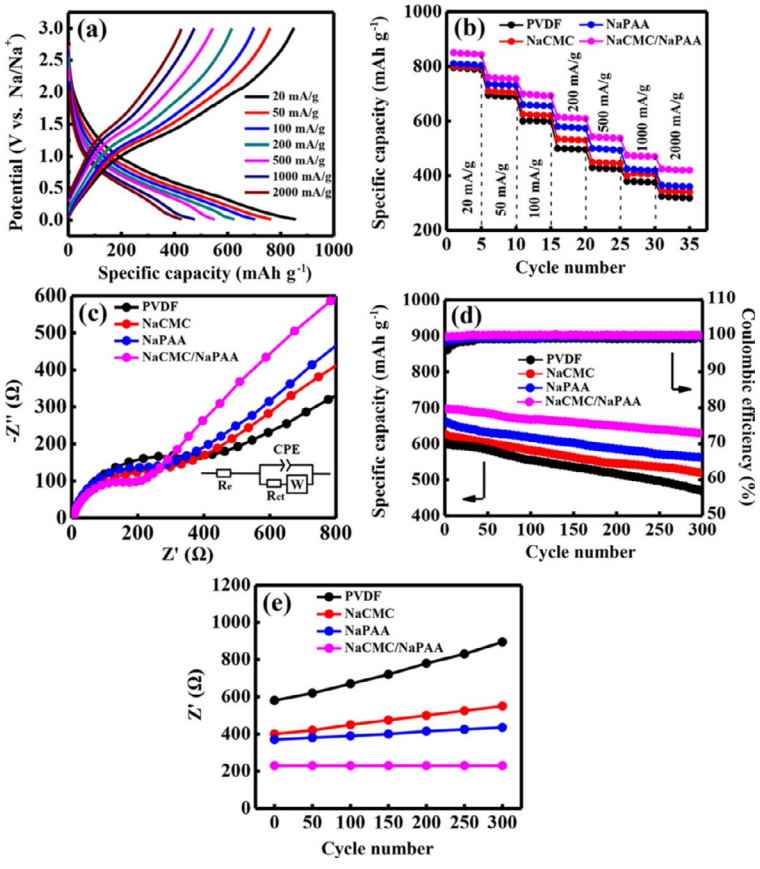


**Figure 5.** (a) Charge–discharge curves of NaCMC/NaPAA electrode measured at various rates. (b) Comparison of reversible capacities of various electrodes measured at various rates. (c) EIS data of the electrodes with various binders after conditioning cycles. (d) Cycling stability data of $SnO_2$@CMK-8 electrodes with various binders measured at 100 mA g$^{-1}$. (e) $R_{ct}$ values of various electrodes with respect to charge–discharge cycle number.

The binder effects on the rate capability of the $SnO_2$@CMK-8 electrodes are shown in Figure 5b. At a high rate of 2000 mA g$^{-1}$, the electrodes with PVDF, NaCMC, NaPAA, and NaCMC/NaPAA binders had reversible capacities of 325, 345, 365, and 425 mAh g$^{-1}$, corresponding to 41%, 43%, 45%, and 50% retention, respectively (Table 1), compared with the values measured at 20 mA g$^{-1}$. The reasons for the performance variation were determined using electrochemical impedance spectroscopy (EIS). As revealed in the Nyquist plots in Figure 5c, the spectra consisted of a semicircle at high frequency and a sloping line at low frequency, which can be characterized by the equivalent circuit shown in the inset, in which $R_e$, $R_{ct}$, *CPE*, and *W* are the electrolyte resistance, interfacial charge transfer resistance, interfacial constant phase element, and Warburg impedance associated with $Na^+$ diffusion in the electrode, respectively.[30] The $R_{ct}$ values, which are related to the EIS semicircle diameter, were calculated to be 580, 400, 370, and 240 Ω for the PVDF, NaCMC, NaPAA, and NaCMC/NaPAA electrodes, respectively. The higher $R_{ct}$ of the PVDF electrode was attributed to its thicker SEI layer (Figure 3c). The apparent $Na^+$ diffusion coefficients ($D_{Na^+}$) for the electrodes were calculated from the oblique linear Warburg parts;[64] the calculated values for these electrodes were $1.7\times10^{-16}$, $3.8\times10^{-15}$, $6.1\times10^{-15}$, and $8.3\times10^{-15}$ cm$^2$ s$^{-1}$, respectively. The tightly packed $SnO_2$@CMK-8 NPs can form a favorable $Na^+$ diffusion pathway, which resulted in an enhanced transport rate. The $D_{Na^+}$

values of the PVDF and NaCMC/NaPAA electrodes were also estimated using CV (see Figure S9 for details). The linear relationship between the redox current and the square root of the CV sweep rate indicated that the sodiation/desodiation reactions were diffusion-controlled. The obtained $D_{Na^+}$ values were $7.2\times10^{-16}$ and $1.2\times10^{-14}$ $cm^2 s^{-1}$, respectively, which were consistent with the EIS data, again confirming the importance of the binder selection for achieving the desired electrochemical properties.

The cycling stability of the various $SnO_2$@CMK-8 electrodes was evaluated at 100 mA $g^{-1}$; the results are shown in Figure 5d. The capacity retention ratios after 300 cycles were 78%, 83%, 85%, and 90% for the PVDF, NaCMC, NaPAA, and NaCMC/NaPAA electrodes, respectively (Table 1), with the CE values saturating at 98.6%, 99.1%, 99.2%, and 99.7%, respectively. The variation of $R_{ct}$ with the number of cycles for the electrodes is shown in Figure 5e. The more pronounced $R_{ct}$ increase upon cycling for the PVDF electrode indicated the inferior surface passivation of this electrode. The accumulation of the SEI layer, which not only increased the electrode resistance but also decreased the number of electroactive sites, led to the capacity fading. In contrast, the adhesive and dispersant nature of NaCMC,[11] when mixed with NaPAA, improved the wetting and spreading of the binder on the active particle surface. This artificial layer that formed was robust and could suppress the SEI evolution, improving the electrode durability. The cycling stability of the electrodes was further examined at a high charge–discharge rate of 2000 mA $g^{-1}$ (Figure S10). After 150 cycles, the capacity retention ratios were 56%, 64%, 66%, and 73% for the PVDF, NaCMC, NaPAA, and NaCMC/NaPAA electrodes, respectively. The decreased durability at a high sodiation-desodiation rate suggested that the electrode volume expansion/shrinkage, rather than other parasitic reactions, was mainly responsible for the capacity decay. A good binder, even though it accounts for only a small portion of the electrode, plays a significant role in cycling stability, especially under high-rate operation. Besides the binder selection, the electrode cycling stability can also be improved by development of new electrolyte formulations, electrode architectures, and other pretreatment processes.[16,70,71]

Figure S11 compares the surface appearances of the electrodes after 300 charge–discharge cycles. For the PVDF electrode, some of the Cu substrate was exposed (owing to the detachment of the active material layer), whereas the NaCMC/NaPAA electrode retained the best mechanical integrity. The corresponding electrode morphologies examined using SEM are shown in Figure 6. The PVDF electrode had huge cracks and was covered by a thick SEI layer. The PVDF binder could not withstand the substantial electrode volume change during cycling (Figures 6a), leading to decohesion and pulverization (see the focused ion beam (FIB) cross-section image in Figure 6e). As shown in Figures 6b and c, thinner SEI layers and smaller cracks were observed for the NaCMC and NaPAA electrodes. The highest structural stability was observed for the electrode with NaCMC/NaPAA mixed binder (Figure 6d). The types of groups on the polymer chains of NaCMC are different from those of NaPAA (Figure S1) and could provide extra

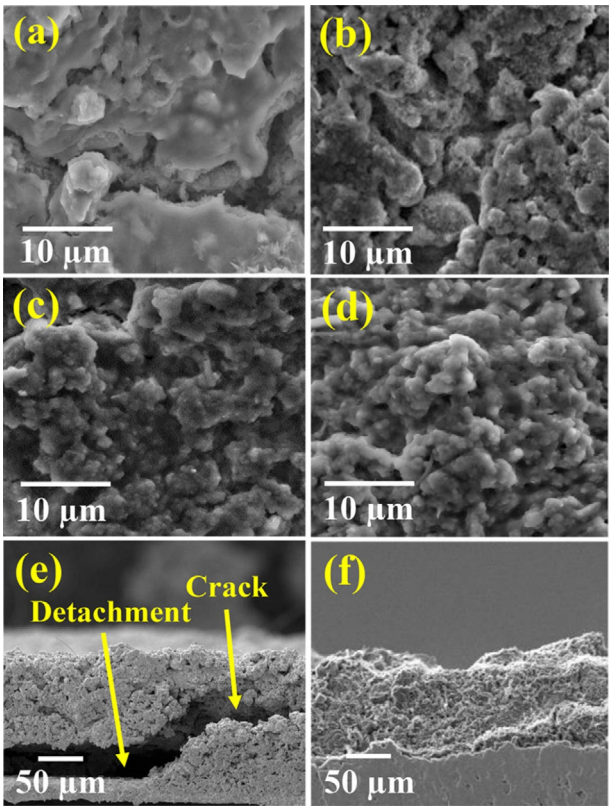


**Figure 6.** SEM images of $SnO_2$@CMK-8 electrodes with (a) PVDF, (b) NaCMC, (c) NaPAA, and (d) NaCMC/NaPAA binders after 300 charge–discharge cycles. FIB cross-section images of (e) PVDF and (f) NaCMC/NaPAA electrodes after the same cycles.

bonding sites. Moreover, NaCMC can act as a dispersant to enhance the uniformity of NaPAA in the electrode slurry.[11,53] As revealed in the cross-section micrograph (Figure 6f), the active material layer was tightly adhered to the current collector. This confirmed that NaCMC/NaPAA mixed binder can buffer the electrode mechanical stress during cycling and maintain the structural integrity, suppressing the growth of the SEI layer.

The stability of the polymer binders was also examined by soaking it in the electrolyte; the results are shown in Figure S12. The PVDF powder was easily peptized by the electrolyte. This implied that the structural firmness and the conductive pathways of the PVDF electrode can be degraded by electrolyte penetration, especially with high-expansion electrode materials. In contrast, the other water-soluble binders were quite stable in the organic electrolyte and settled down well under the vessels. This property is important for sustaining a robust electrode framework. The stable NaCMC and NaPAA binders can also serve as barrier layers to reduce undesirable parasitic reactions between the $SnO_2$@CMK-8 electrode and the electrolyte.

The $SnO_2$@CMK-8 powder was scraped from the PVDF and NaCMC/NaPAA electrodes after 300 charge–discharge cycles and then subjected to TEM analyses. As shown in Figure 7, for the PVDF sample, the $SnO_2$ NPs had escaped from the CMK-8 matrix, leading to agglomeration and separation of the oxide. In contrast, with the NaCMC/NaPAA binder, the microstructure

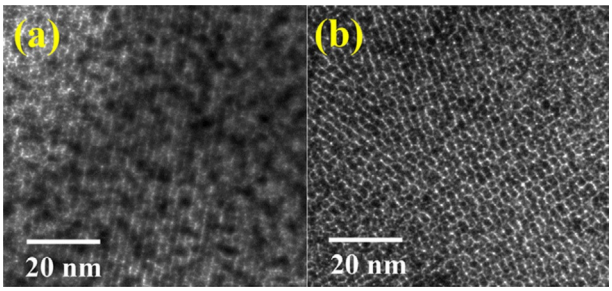


**Figure 7.** TEM images of $SnO_2$@CMK-8 samples with (a) PVDF and (b) NaCMC/NaPAA binders after 300 charge–discharge cycles.

of $SnO_2$@CMK-8 was well preserved. These results suggest that the binder can effectively wrap the $SnO_2$@CMK-8 spheres and keep the $SnO_2$ NPs encapsulated inside the CMK-8 matrix after cycling (Figure 4). The conducting network and electroactive sites for $SnO_2$ can be retained, leading to excellent cycling stability of the electrode.

Figure 8 shows the thermal reactivity of the sodiated electrodes with various binders examined with DSC. In general, the following reactions can be distinguished in the DSC profiles with increasing temperature: the original SEI film breakdown,

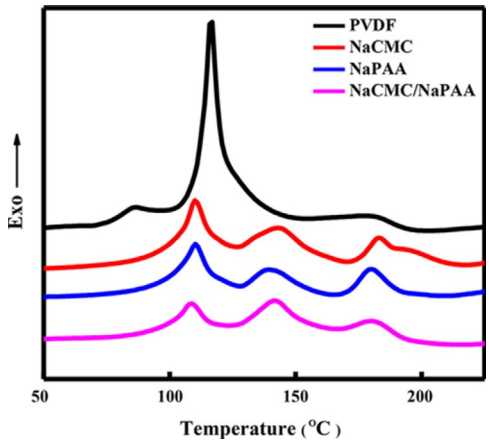


**Figure 8.** DSC data of sodiated $SnO_2$@CMK-8 samples with various binders.

the chemical reaction between the electrolyte and the SEI-free sodiated anode (leading to the formation of a new SEI layer), and the thermal decomposition of this reformed SEI layer.[47,48] The original SEI layer of the PVDF electrode decomposed at the lowest temperature (Table 2) with the least heat released. These data indicate that the SEI chemistry is indeed altered by the electrode binder. The reasons for the more exothermic SEI decomposition reactions of the aqueous binder electrodes are unknown; this topic requires further investigation. Interestingly, the reaction enthalpies of the SEI-free anodes and electrolyte (the second DSC peaks) were significantly reduced with the use of the aqueous binders, especially NaCMC/NaPAA. It is believed that the binder layer, which effectively wets the electrode surface, can decrease the direct contact of the electrode with the electrolyte, suppressing the reactivity. The total heat

**Table 2.** DSC data of sodiated $SnO_2$@CMK-8 anodes with various binders evaluated in a temperature range of 50–225 °C.

| Binders | Exothermic onset temperature [°C] | Total heat released [J g$^{-1}$] |
|---|---|---|
| PVDF | 75 | 300 |
| NaCMC | 101 | 247 |
| NaPAA | 101 | 232 |
| NaCMC/NaPAA | 100 | 195 |

generated, summarized in Table 2, for the PVDF, NaCMC, NaPAA, and NaCMC/NaPAA samples was 300, 247, 232, and 195 J g$^{-1}$, respectively, up to 225 °C. The binder effects on the electrode safety characteristics were demonstrated for NIB applications for the first time in this study.

## Conclusions

Binder selection was found to be crucial for optimizing the electrochemical performance of a $SnO_2$@CMK-8 anode for NIBs. A NaCMC/NaPAA binder, which was stable in the electrolyte, could effectively wet, spread on the surfaces, and tightly glue the $SnO_2$@CMK-8 particles, increasing the adhesion strength and compressed density of the active material layer. This mixed binder (with synergistic effects) not only withstood the electrode volume variation and maintained structural integrity upon cycling, but also formed a protective layer on the electrode to separate the liquid electrolyte with the active particles and suppressed the growth of the SEI layer. A reduced $R_{ct}$ and increased $D_{Na^+}$ were also found for this electrode, which showed excellent capacity (850 mAh g$^{-1}$ or 326 mAh cm$^{-1}$), rate capability (425 mAh g$^{-1}$@2000 mAh g$^{-1}$), and cycling stability (90% capacity retention after 300 cycles). The use of NaCMC/NaPAA binder also increased the exothermic onset temperature and reduced the total heat generated at the anode, improving the NIB safety. This cost-effective binder has great practical potential for NIB applications.

## Experimental Section

### Synthesis of $SnO_2$@CMK-8 and cell assembly

$SnO_2$@CMK-8 was synthesized using procedures described in our previous study.[32] PVDF (Sigma–Aldrich), NaCMC (Sigma–Aldrich), and NaPAA (Kishida Chemicals) binders were used as received. The molecular structures of the binders are shown in Figure S1. The electrode slurry was made up of 80 wt% $SnO_2$@CMK-8, 10 wt% carbon black, and 10 wt% binder dispersed in either *N*-methyl-2-pyrrolidone (for PVDF) or distilled water [for NaCMC, NaPAA, and NaCMC/NaPAA (1:1 by weight)]. The slurry was coated onto Cu foil with a doctor blade and dried at 100 °C for 3 h under vacuum. The final thickness of the active material layers was approximately 65 μm. The active material loading was typically 1–1.2 mg cm$^{-2}$. This electrode was roll-pressed and then punched to match the required dimensions of a CR2032 coin cell. We did not find any considerable impact of the binder mixing sequence on the electrochemical properties of the NaCMC/NaPAA electrodes. A thick Na foil and a glassy fiber membrane were used as the counter electrode and separator, respectively. The electrolyte was 1 M $NaClO_4$ in

propylene carbonate (PC)/ethylene carbonate (EC) mixed solvent (1:1 by volume) with 5 wt% fluoroethylene carbonate (FEC) additive. The assembly of the coin cells was performed in an argon-filled glove box (Innovation Technology Co. Ltd.), in which both the moisture and oxygen content levels were maintained at below 0.5 ppm.

### Material and electrochemical characterization

The crystallinity of $SnO_2$@CMK-8 was characterized by X-ray diffraction (XRD; Bruker D8 ADVANCE) using $Cu_{K\alpha}$ radiation as the incident X-ray source. The small-angle XRD patterns were recorded with a Shimadzu LabX XRD-6000 diffractometer with $Cu_{K\alpha}$ radiation. The morphology and microstructure of the samples were examined using SEM (FEI Inspect F50), a FIB; FEI V ersa 3D), and high-resolution TEM (TEM; JEOL 2100F). X-ray photoelectron spectroscopy (XPS; VG Sigma Probe) was used to analyze the surface chemical compositions of the electrodes. $Al_{K\alpha}$ radiation (1486.6 eV) was used as the excitation source. All of the acquired spectra were referenced to the C 1s peak of hydrocarbon at a binding energy of 284.6 eV. XPSPEAK 4.1 software was adopted for the data fitting. TGA (PerkinElmer TGA7) were conducted with a heating rate of 5 °C min$^{-1}$ to characterize the thermal stability of the binders. EIS was performed in the frequency range of 100 kHz-10 mHz with an AC amplitude of 10 mV. A Biologic VSP-300 potentiostat was used for CV measurements. The charge–discharge properties (such as capacity, rate performance, and cycling stability) of various electrodes were evaluated using a battery tester (Arbin, BT-2043) at 25 °C. For each condition, at least five coin cells were tested. The performance deviation was typically within 5%. The reported data are the median values. The thermal reactivity of the sodiated $SnO_2$@CMK-8 samples with various binders was evaluated using DSC (Netzsch DSC3500) in a temperature range of 50–225 °C. The samples were presodiated to 0.01 V versus Na/Na$^+$, recovered from the coin cells, placed into Al capsules in the glove box without washing and drying, and then transferred to the DSC chamber, which was filled with $N_2$ gas and heated at a rate of 10 °C min$^{-1}$.

## Acknowledgements

*The financial support provided for this work by the Ministry of Science and Technology (MOST) of Taiwan is gratefully appreciated. JL acknowledges the support provided by the National Science Foundation (ECCS-1610806).*

## *Conflict of interest*

*The authors declare no conflict of interest.*

**Keywords:** batteries · binders · electrodes · energy storage · sodium

[1] J. W. Choi, D. Aurbach, *Nat. Rev. Mater.* **2016**, *1*, 16013.
[2] H. Kim, H. Kim, Z. Ding, M. H. Lee, K. Lim, G. Yoon, K. Kang, *Adv. Energy Mater.* **2016**, *6*, 1600943.
[3] C. Vaalma, D. Buchholz, M. Weil, S. Passerini, *Nat. Rev. Mater.* **2018**, *3*, 18013.
[4] N. Wongittharom, C. H. Wang, Y. C. Wang, C. H. Yang, J. K. Chang, *ACS Appl. Mater. Interfaces* **2014**, *6*, 17564 – 17570.
[5] C. H. Wang, Y. W. Yeh, N. Wongittharom, Y. C. Wang, C. J. Tseng, S. W. Lee, W. S. Chang, J. K. Chang, *J. Power Sources* **2015**, *274*, 1016 – 1023.
[6] H. Y. Li, C. H. Yang, C. M. Tseng, S. W. Lee, C. C. Yang, T. Y. Wu, J. K. Chang, *J. Power Sources* **2015**, *285*, 418 – 424.
[7] Y. You, A. Manthiram, *Adv. Energy Mater.* **2018**, *8*, 1701785.
[8] P. K. Nayak, L. Yang, W. Brehm, P. Adelhelm, *Angew. Chem. Int. Ed.* **2018**, *57*, 102 – 120; *Angew. Chem.* **2018**, *130*, 106 – 126.
[9] P. Ge, M. Fouletier, *Solid State Ionics* **1988**, *28 – 30*, 1172 – 1175.
[10] B. Jache, P. Adelhelm, *Angew. Chem. Int. Ed.* **2014**, *53*, 10169 – 10173; *Angew. Chem.* **2014**, *126*, 10333 – 10337.
[11] W. Zhang, M. Dahbi, S. Komaba, *Curr. Opin. Chem. Eng.* **2016**, *13*, 36 – 44.
[12] C. Bommier, X. Ji, *Small* **2018**, *14*, 1703576.
[13] S. Komaba, T. Ishikawa, N. Yabuchi, W. Murata, A. Ito, Y. Ohsawa, *ACS Appl. Mater. Interfaces* **2011**, *3*, 4165 – 4168.
[14] P. Arora, Z. Zhang, *Chem. Rev.* **2004**, *104*, 4419 – 4462.
[15] Q. Zhang, Z. Yu, P. Du, C. Su, *Recent Pat. Nanotechnol.* **2010**, *4*, 100 – 110.
[16] J. Y. Hwang, S. T. Myung, Y. K. Sun, *Chem. Soc. Rev.* **2017**, *46*, 3529 – 3614.
[17] S. L. Chou, Y. Pan, J. Z. Wang, H. K. Liu, S. X. Dou, *Phys. Chem. Chem. Phys.* **2014**, *16*, 20347 – 20359.
[18] J. T. Li, Z. Y. Wu, Y. Q. Lu, Y. Zhou, Q. S. Huang, L. Huang, S. G. Sun, *Adv. Energy Mater.* **2017**, *7*, 1701185.
[19] N. Yabuuchi, K. Kubota, M. Dahbi, S. Komaba, *Chem. Rev.* **2014**, *114*, 11636 – 11682.
[20] X. Wang, C. Yao, F. Wang, Z. Li, *Small* **2017**, *13*, 1702240.
[21] M. Dahbi, T. Nankano, N. Yabuchi, T. Ishikawa, K. Kubota, M. Fukunishi, S. Shibahara, J. Y. Son, Y. T. Cui, H. Oji, S. Komaba, *Electrochem. Commun.* **2014**, *44*, 66 – 69.
[22] Y. Shi, X. Zhou, G. Yu, *Acc. Chem. Res.* **2017**, *50*, 2642 – 2652.
[23] S. Komaba, K. Okushi, T. Ozeki, H. Yui, Y. Katayama, T. Miura, T. Saito, H. Groult, *Electrochem. Solid-State Lett.* **2009**, *12*, A107 – A110.
[24] J. Zhao, X. Yang, Y. Yao, Y. Gao, Y. Sui, B. Zou, H. Ehrenberg, G. Chen, F. Du, *Adv. Sci.* **2018**, *5*, 1700768.
[25] V. Dall'Asta, D. Buchholz, L. G. Chagas, X. Dou, C. Ferrara, E. Quartarone, C. Tealdi, S. Passerini, *ACS Appl. Mater. Interfaces* **2017**, *9*, 34891 – 34899.
[26] K. Chen, W. Zhang, L. Xie, W. Chen, X. Xiang, M. Wan, Y. Huang, *ACS Appl. Mater. Interfaces* **2017**, *9*, 1536 – 1541.
[27] S. Y. Hong, Y. Kim, Y. Park, A. Choi, N. S. Choi, K. T. Lee, *Energy Environ. Sci.* **2013**, *6*, 2067 – 2081.
[28] Z. Li, J. Ding, D. Mitlin, *Acc. Chem. Res.* **2015**, *48*, 1657 – 1665.
[29] B. Huang, Z. Pan, X. Su, L. An, *J. Power Sources* **2018**, *395*, 41 – 59.
[30] J. Patra, H. C. Chen, C. H. Yang, C. T. Hsieh, C. Y. Su, J. K. Chang, *Nano Energy* **2016**, *28*, 124 – 134.
[31] X. Li, Z. Zhu, G. P. Nayaka, J. Duan, D. Wang, P. Dong, L. Huang, J. Zhao, S. Sun, X. Yu, Y. Zhang, *J. Alloys Compd.* **2018**, *752*, 68 – 75.
[32] J. Patra, P. C. Rath, C. H. Yang, D. Saikia, H. M. Kao, J. K. Chang, *Nanoscale* **2017**, *9*, 8674 – 8683.
[33] R. Ryoo, S. H. Joo, *Stud. Surf. Sci. Catal.* **2004**, *148*, 241 – 260.
[34] P. C. Rath, J. Patra, D. Saikia, M. Mishra, J. K. Chang, H. M. Kao, *J. Mater. Chem. A* **2016**, *4*, 14222 – 14233.
[35] Y. Y. Wang, B. H. Hou, Y. N. Wang, H. Y. Lu, J. Z. Guo, Q. L. Ning, J. P. Zhang, C. L. Lu, X. L. Wu, *J. Mater. Chem. A* **2018**, *6*, 6578 – 6586.
[36] M. Dirican, Y. Lu, Y. Ge, O. Yildiz, X. Zhang, *ACS Appl. Mater. Interfaces* **2015**, *7*, 18387 – 18396.
[37] H. Z. Li, L. Y. Yang, J. Liu, S. T. Li, L. B. Fang, Y. K. Lu, H. R. Yang, S. L. Liu, M. Lei, *J. Power Sources* **2016**, *324*, 780 – 787.
[38] Y. Wei, Z. Wang, H. Ye, J. Mou, D. Lei, Y. Liu, W. Lv, B. Li, F. Kang, Y. B. He, *ChemistrySelect* **2017**, *2*, 11365 – 11369.
[39] Z. Zhu, F. Liang, Z. Zhou, X. Zeng, D. Wang, P. Dong, J. Zhao, S. Sun, Y. Zhang, X. Li, *J. Mater. Chem. A* **2018**, *6*, 1513 – 1522.
[40] Y. Zhang, H. Hou, X. Yang, J. Chen, M. Jing, Z. Wu, X. Jia, X. Ji, *J. Power Sources* **2016**, *305*, 200 – 208.
[41] J. Song, Z. Yu, M. L. Gordin, X. Li, H. Peng, D. Wang, *ACS Nano* **2015**, *9*, 11933 – 11941.
[42] Y. Zhang, M. Ji, Z. Liu, Y. He, Y. Hu, Q. Yang, B. Lia, J. Wang, *RSC Adv.* **2017**, *7*, 25678 – 25684.
[43] M. J. Piernas-Muñoz, E. C. Martinez, J. L. G. Camer, T. Rojo, *Electrochim. Acta* **2016**, *200*, 123 – 130.
[44] Z. J. Han, K. Yamagiwa, N. Yabuuchi, J. Y. Son, Y. T. Cui, H. Oji, A. Kogure, T. Harada, S. Ishikawa, Y. Aoki, S. Komaba, *Phys. Chem. Chem. Phys.* **2015**, *17*, 3783 – 3795.
[45] Q. Fan, W. Zhang, J. Duan, K. Hong, L. Xue, Y. Huang, *Electrochim. Acta* **2015**, *174*, 970 – 977.

[46] Y. Yui, M. Hayashi, K. Hayashi, J. Nakamura, *Solid State Ionics* **2016**, *288*, 219 – 223.
[47] A. Ponrouch, E. Marchante, M. Courty, J. M. Tarascona, M. R. Palacın, *Energy Environ. Sci.* **2012**, *5*, 8572 – 8583.
[48] G. G. Eshetu, S. Grugeon, H. Kim, S. Jeong, L. Wu, G. Gachot, S. Laruelle, M. Arman, S. Passerini, *ChemSusChem* **2016**, *9*, 462 – 471.
[49] Y. S. Park, E. S. Oh, S. M. Lee, *J. Power Sources* **2014**, *248*, 1191 – 1196.
[50] F. Kleitz, S. H. Choi, R. Ryoo, *Chem. Commun.* **2003**, 2136 – 2137.
[51] N. Cuesta, A. Romes, I. Camean, C. Antuna, A. B. Garcia, *Electrochim. Acta* **2015**, *155*, 140 – 147.
[52] N. P. W. Pieczonka, V. Borgel, B. Ziv, N. Leifer, V. Dargel, D. Aurbach, J. H. Kim, Z. Liu, X. Huang, S. A. Krachkovskiy, G. R. Goward, I. Halalay, B. R. Powell, A. Manthiram, *Adv. Energy Mater.* **2015**, *5*, 1501008.
[53] L. Chen, X. Xie, J. Xie, K. Wang, J. Yang, *J. Appl. Electrochem.* **2006**, *36*, 1099 – 1104.
[54] H. Gao, B. Ji, I. L. Jager, E. Arzt, P. Fratzl, *Proc. Natl. Acad. Sci. USA* **2003**, *100*, 5597 – 5600.
[55] H. C. Chen, J. Patra, S. W. Lee, C. J. Tseng, T. Y. Wu, M. H. Lin, J. K. Chang, *J. Mater. Chem. A* **2017**, *5*, 13776 – 13784.
[56] J. W. Wang, X. H. Liu, S. X. Mao, J. Y. Huang, *Nano Lett.* **2012**, *12*, 5897 – 5902.
[57] V. L. Chevrier, G. Ceder, *J. Electrochem. Soc.* **2011**, *158*, A1011 – A1014.
[58] J. Ding, H. Wang, Z. Li, A. Kohandehghan, K. Cui, Z. Xu, B. Zahiri, X. Tan, E. M. Lotfabad, B. C. Olsen, D. Mitlin, *ACS Nano* **2013**, *7*, 11004 – 11015.
[59] Y. X. Wang, Y. G. Lim, M. S. Park, S. L. Chou, J. H. Kim, H. K. Liu, S. X. Dou, Y. J. Kim, *J. Mater. Chem. A* **2014**, *2*, 529 – 534.
[60] J. Ding, Z. Li, H. Wang, K. Cui, A. Kohandehghan, X. Tan, D. Karpuzovc, D. Mitlin, *J. Mater. Chem. A* **2015**, *3*, 7100 – 7111.
[61] N. Yabuuchi, K. Shimomura, Y. Shimbe, T. Ozeki, J. Y. Son, H. Oji, Y. Katayama, T. Miura, S. Komaba, *Adv. Energy Mater.* **2011**, *1*, 759 – 765.
[62] S. Komaba, N. Yabuchi, T. Ozeki, Z. J. Han, K. Shimomura, H. Yui, Y. Katayama, T. Miura, *J. Phys. Chem. C* **2012**, *116*, 1380 – 1389.
[63] S. Komaba, K. Shimomura, N. Yabuchi, T. Ozeki, H. Yui, K. Konno, *J. Phys. Chem. C* **2011**, *115*, 13487 – 13495.
[64] L. Fan, X. Li, B. Yan, J. Feng, D. Xiong, D. Li, L. Gu, Y. Wen, S. Lawes, X. Sun, *Adv. Energy Mater.* **2016**, *6*, 1502057.
[65] J. Patra, H. T. Huang, W. Xue, C. Wang, A. S. Helal, J. Li, J. K. Chang, *Energy Storage Mater.* **2019**, *16*, 146 – 154.
[66] K. Takada, Y. Yamada, E. Watanabe, J. Wang, K. Sodeyama, Y. Tateyama, K. Hirata, T. Kawasa, A. Yamada, *ACS Appl. Mater. Interfaces* **2017**, *9*, 33802 – 33809.
[67] H. Kim, J. S. Park, S. H. Sahgong, S. Park, J. K. Kim, Y. Kim, *J. Mater. Chem. A* **2014**, *2*, 19584 – 19588.
[68] Y. Ein-Eli, V. R. Koch, *J. Electrochem. Soc.* **1997**, *144*, 2968 – 2973.
[69] X. F. Luo, A. S. Helal, C. T. Hsieh, J. Li, J. K. Chang, *Nano Energy* **2018**, *49*, 515 – 522.
[70] J. Cui, S. Yao, J. K. Kim, *Energy Storage Mater.* **2017**, *7*, 64 – 114.
[71] C. Chen, Y. Wen, X. Hu, X. Ji, M. Yan, L. Mai, P. Hu, B. Shan, Y. Huang, *Nat. Commun.* **2015**, *6*, 6929.

Manuscript received: August 25, 2018
Revised manuscript received: September 21, 2018
Accepted manuscript online: September 24, 2018
Version of record online: November 8, 2018

CHEMISTRY & SUSTAINABILITY
CHEMSUSCHEM
ENERGY & MATERIALS

Supporting Information

# A Water-Soluble NaCMC/NaPAA Binder for Exceptional Improvement of Sodium-Ion Batteries with an $SnO_2$-Ordered Mesoporous Carbon Anode

Jagabandhu Patra,[a, b, f] Purna Chandra Rath,[a, b] Chi Li,[a] Hsien-Ming Kao,[c] Fu-Ming Wang,[d] Ju Li,*[e] and Jeng-Kuei Chang*[a, b, e, f]

cssc_201801962_sm_miscellaneous_information.pdf

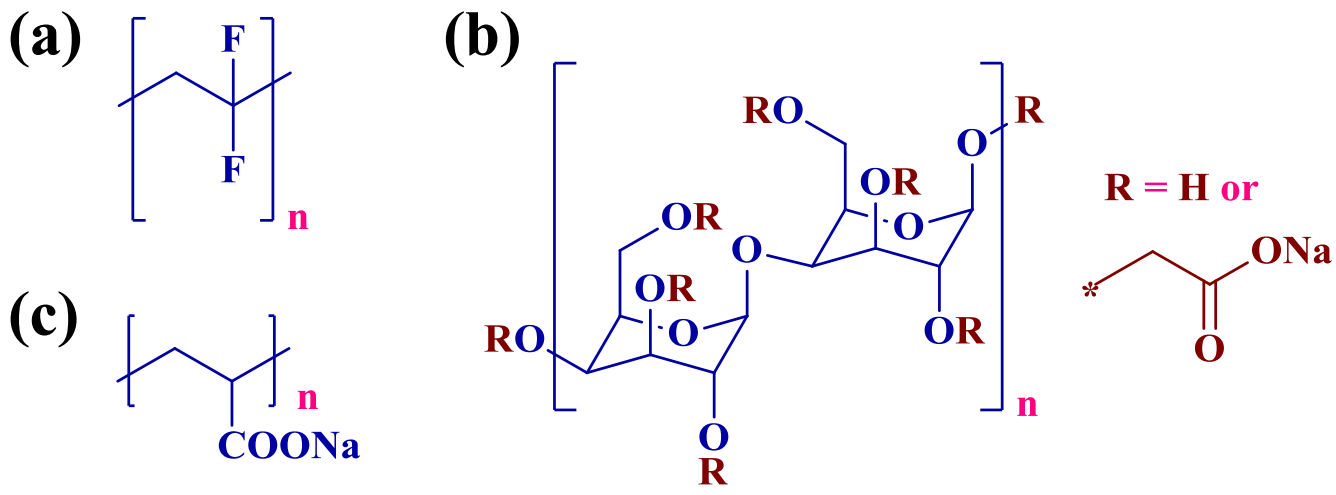


**Figure S1.** Molecular Structures of (a) PVDF, (b) NaCMC, and (c) NaPAA binders.

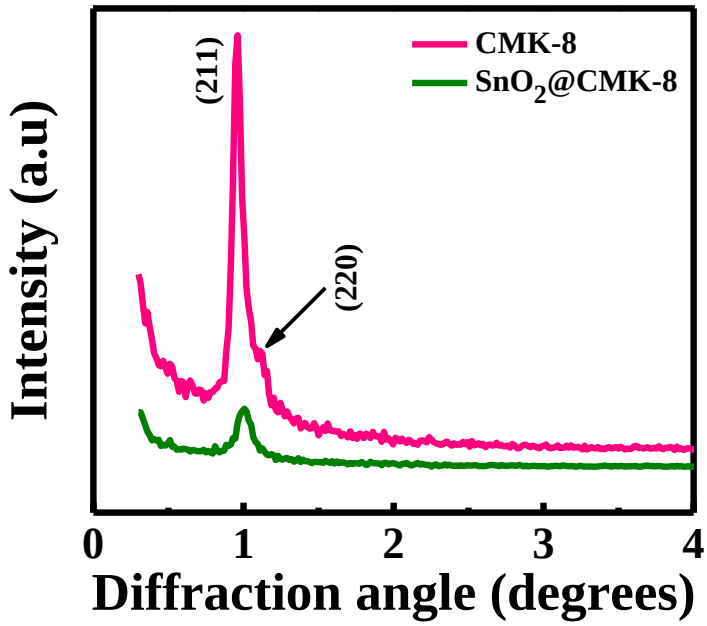


**Figure S2.** Small-angle XRD patterns of pristine CMK-8 and $SnO_2$@CMK-8 composite.

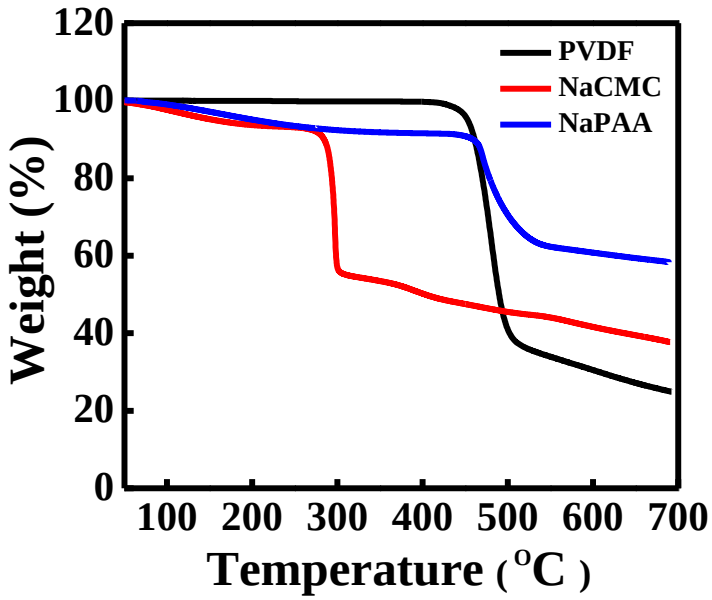


**Figure S3.** TGA data of PVdF, NaCMC, and NaPAA binders measured at a heating rate of 5 °C $min^{-1}$.

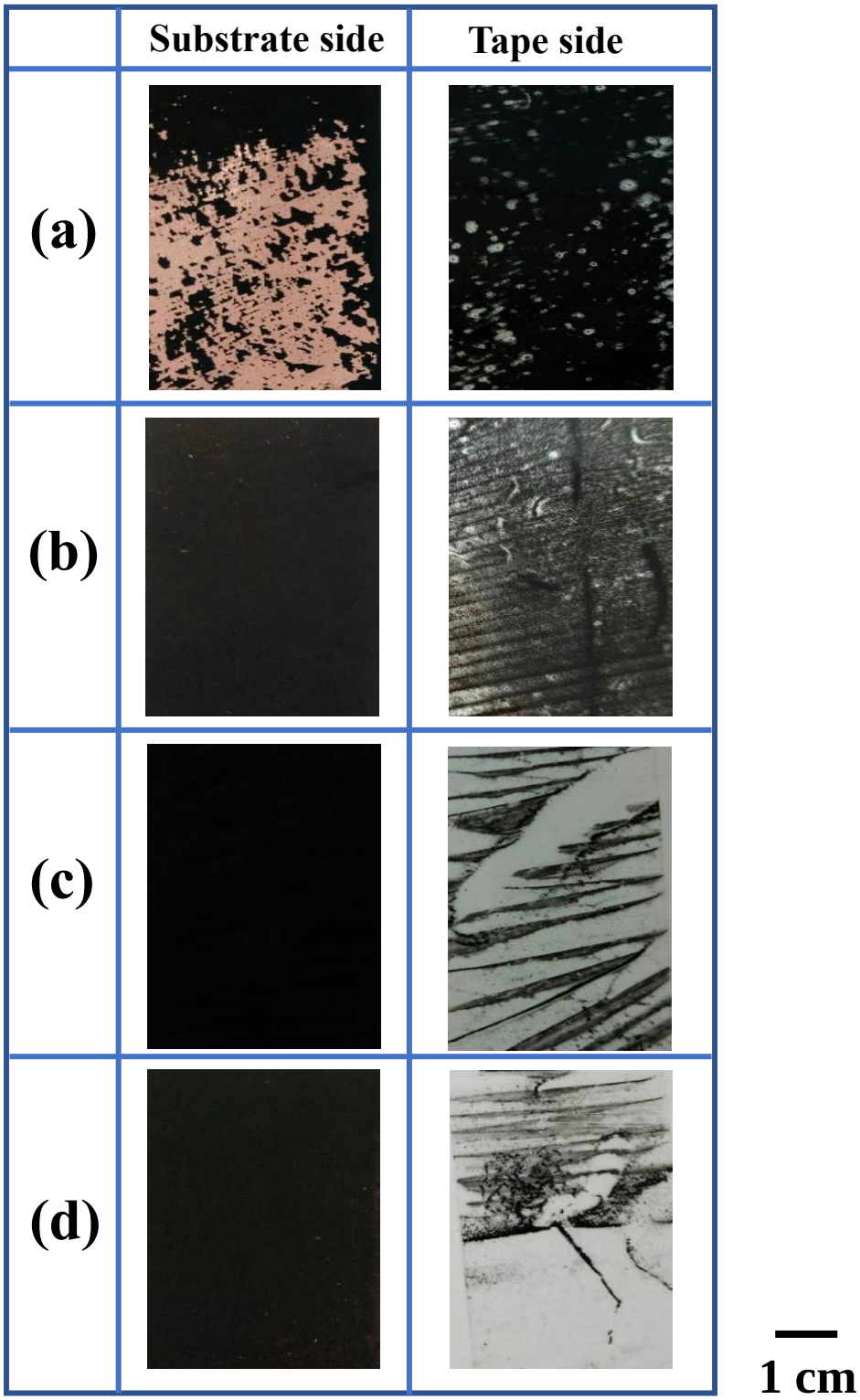


**Figure S4.** Peel test results of $SnO_2$@CMK-8 electrodes with (a) PVDF, (b) NaCMC, (c) NaPAA, and (d) NaCMC/NaPAA electrodes.

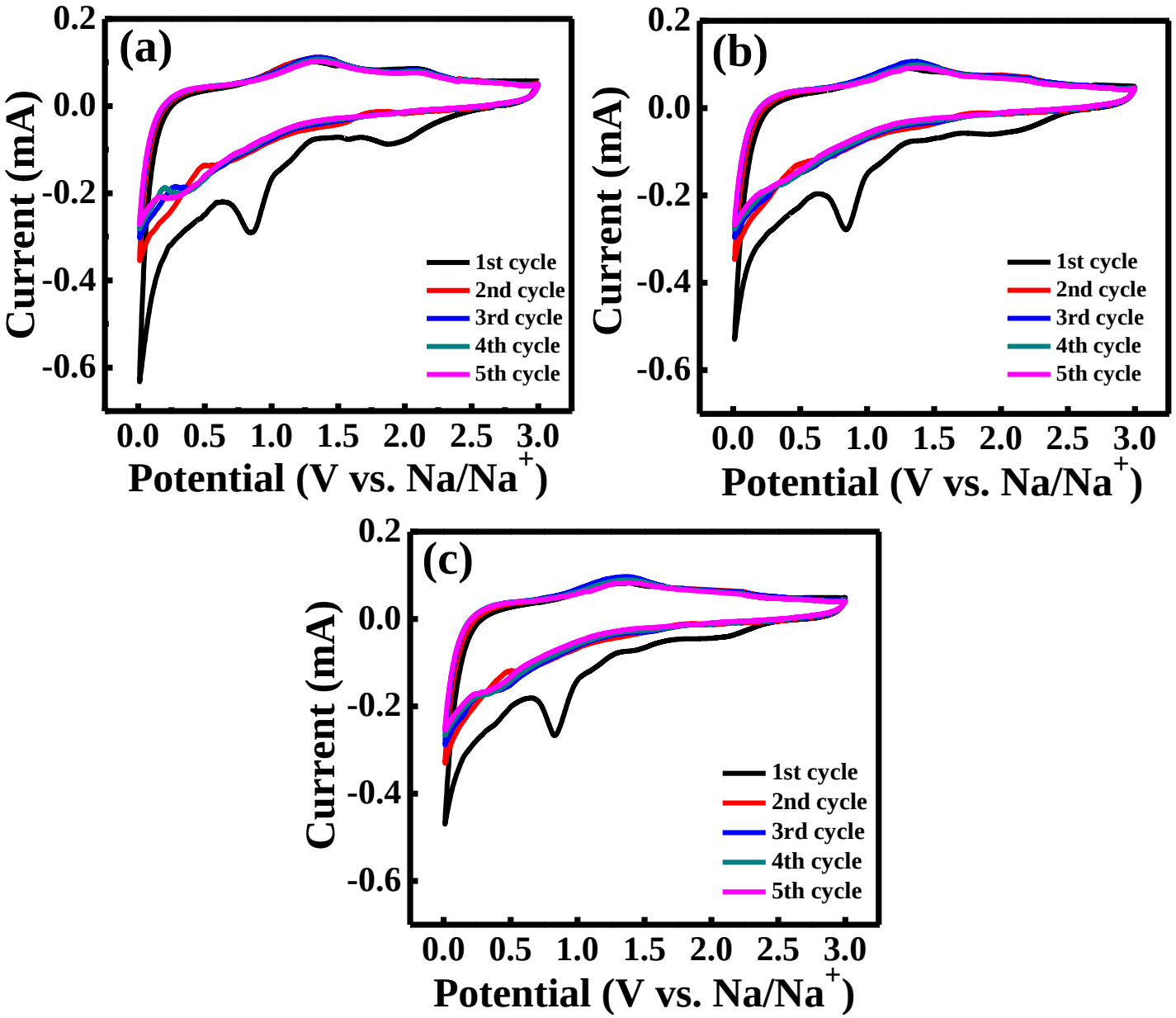


**Figure S5.** CV curves of (a) PVDF, (b) NaCMC, and (c) NaPAA electrodes measured at a scan rate of 0.1 mV $s^{-1}$.

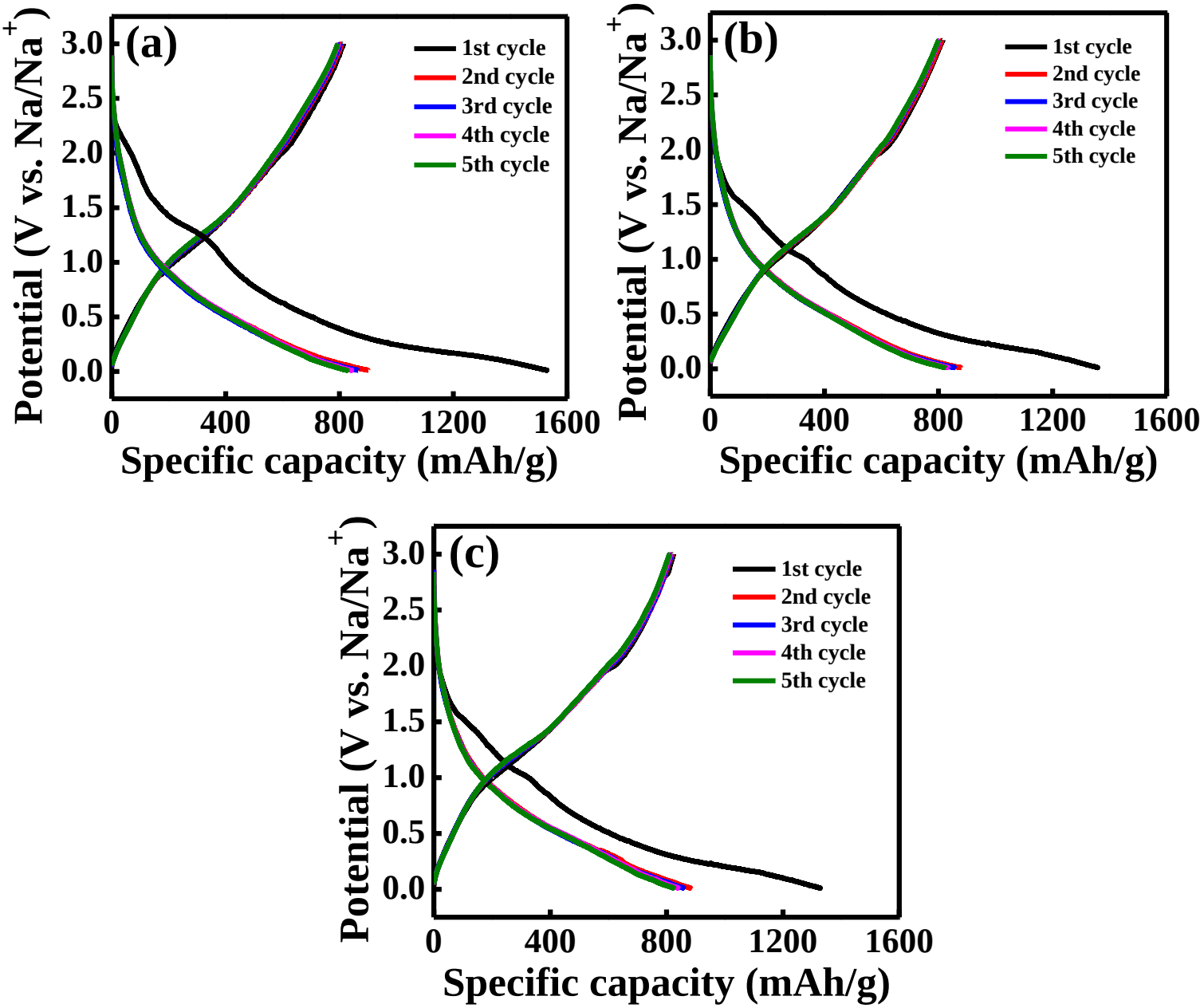


**Figure S6.** Initial five charge–discharge curves of (a) PVDF, (b) NaCMC, and (c) NaPAA electrodes measured at 20 mA $g^{-1}$.

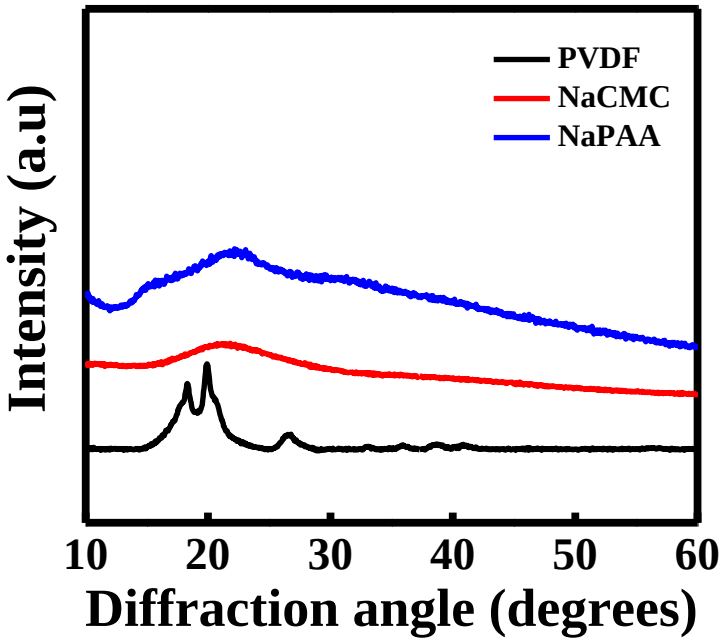


**Figure S7.** XRD patterns of PVDF, NaCMC, and NaPAA binders.

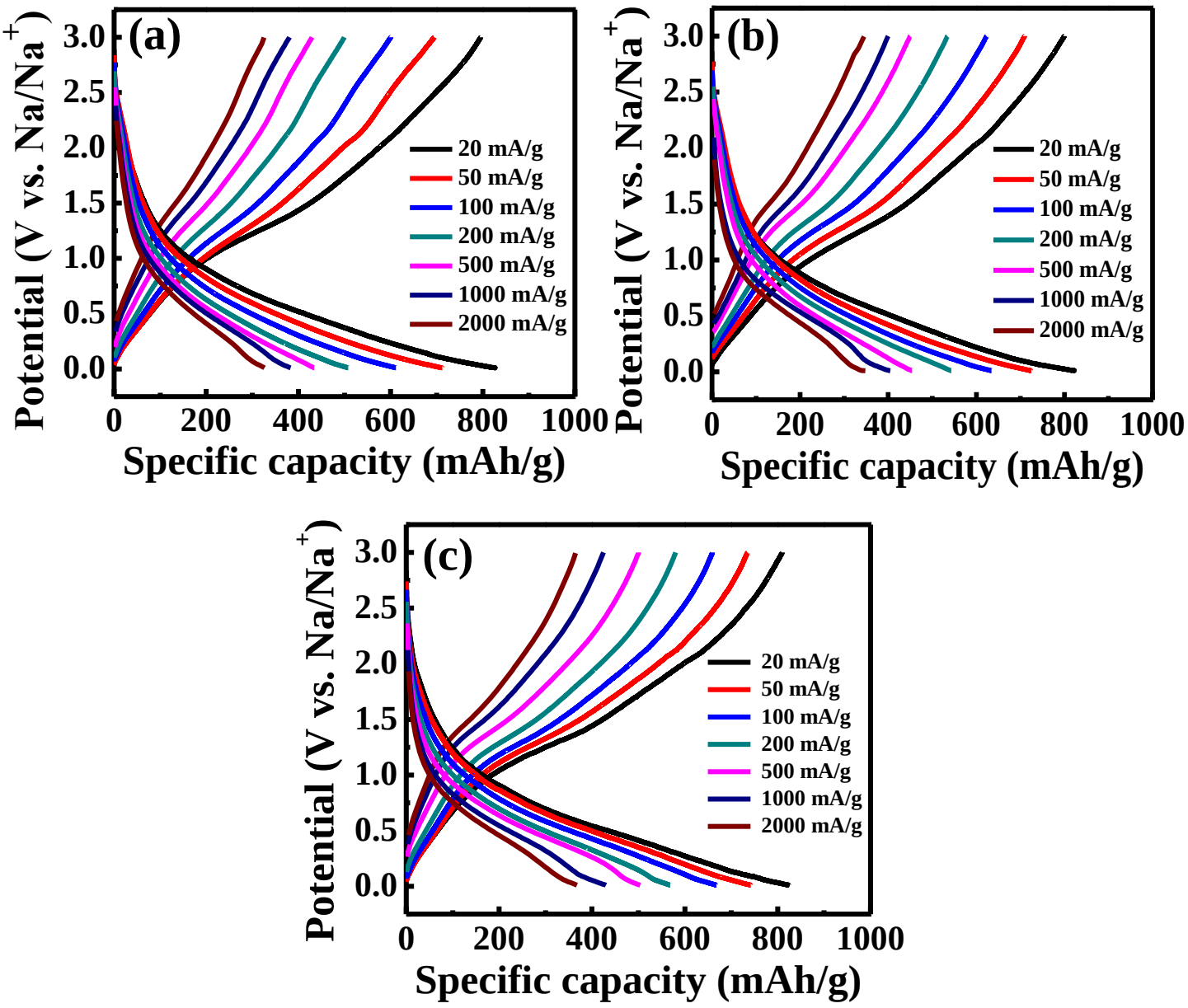


**Figure S8.** Charge−discharge curves of (a) PVDF, (b) NaCMC, and (c) NaPAA electrodes measured at various rates.

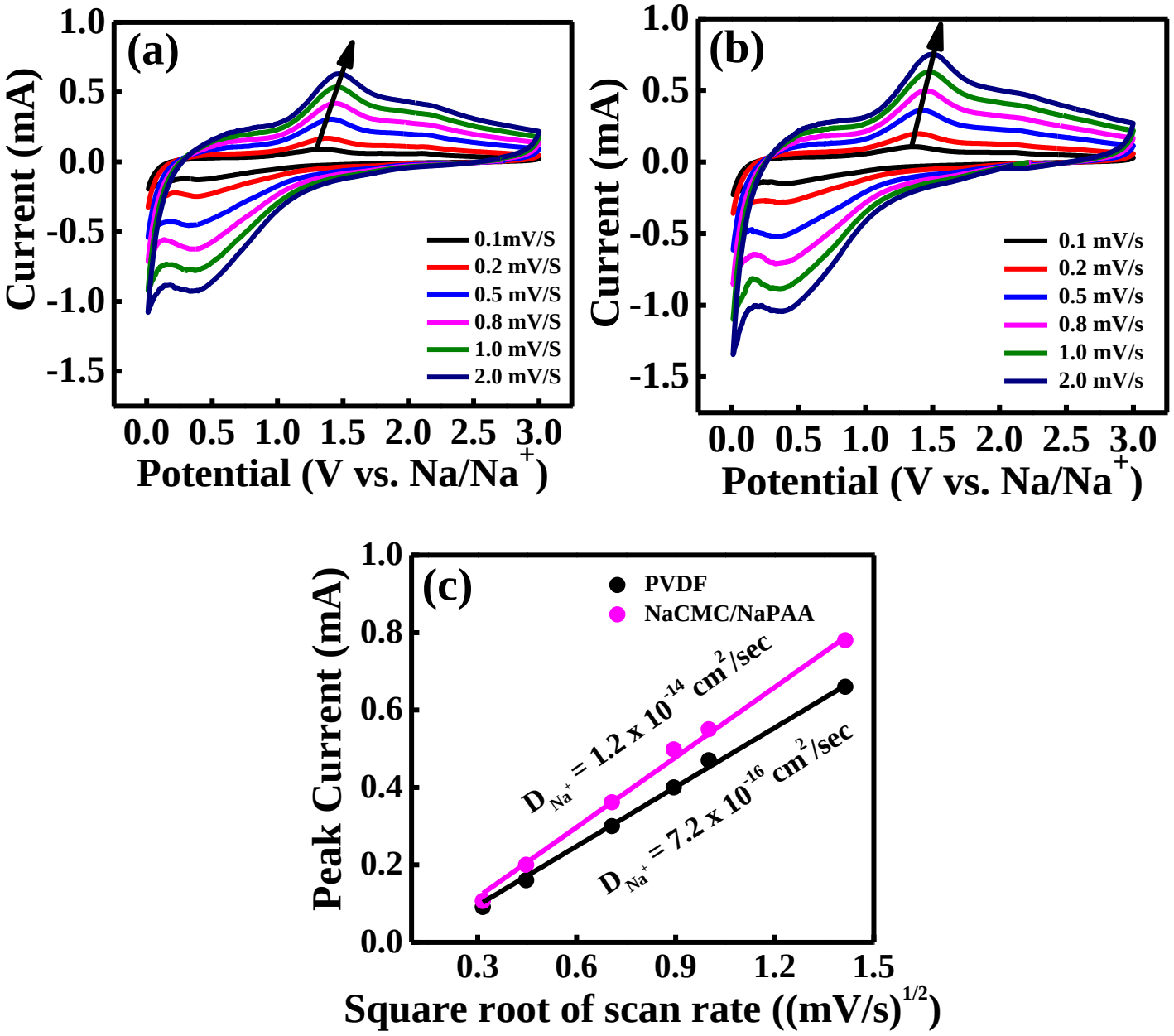


The linear relationship between the redox current and the square root of the CV sweep rate indicates that the sodiation/desodiation reactions are diffusion-controlled. Thus, the following Randles–Sevcik equation is applicable. The apparent $Na^+$ diffusion coefficients can be estimated according to:

$$I_p = (2.69 \times 10^5)\, n^{3/2} A\, D^{1/2} v^{1/2} C_o$$

where $I_p$ is the peak current, $n$ is the charge-transfer number, $A$ is the geometric area of the electrode, $C_o$ is the concentration of $Na^+$ in electrolyte, $v$ is the potential sweep rate, $D$ is the apparent diffusion coefficient of $Na^+$.

**Figure S9.** CV curves of (a) PVDF and (b) NaCMC/NaPAA electrodes measured at various potential sweep rates. (c) $D_{Na^+}$ calculation plots.

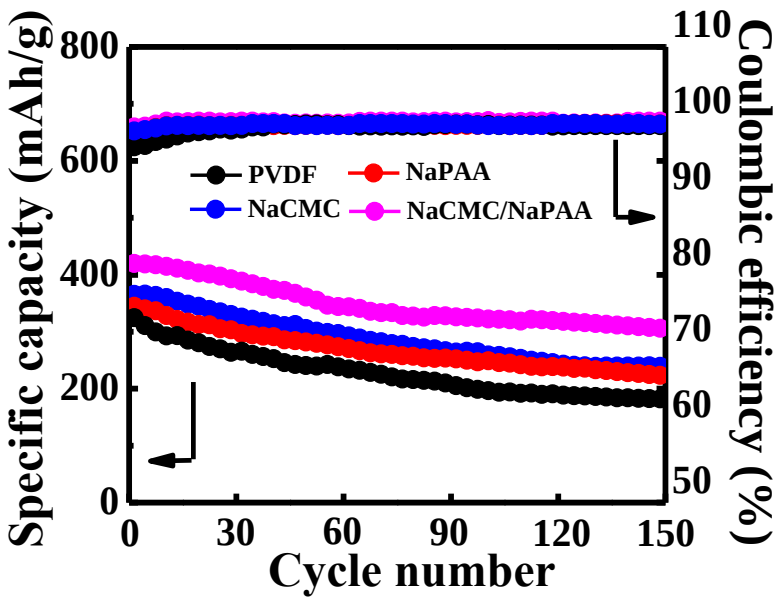


**Figure S10.** Cycling stability data of $SnO_2$@CMK-8 electrodes with various binders measured at 2000 mA $g^{-1}$.

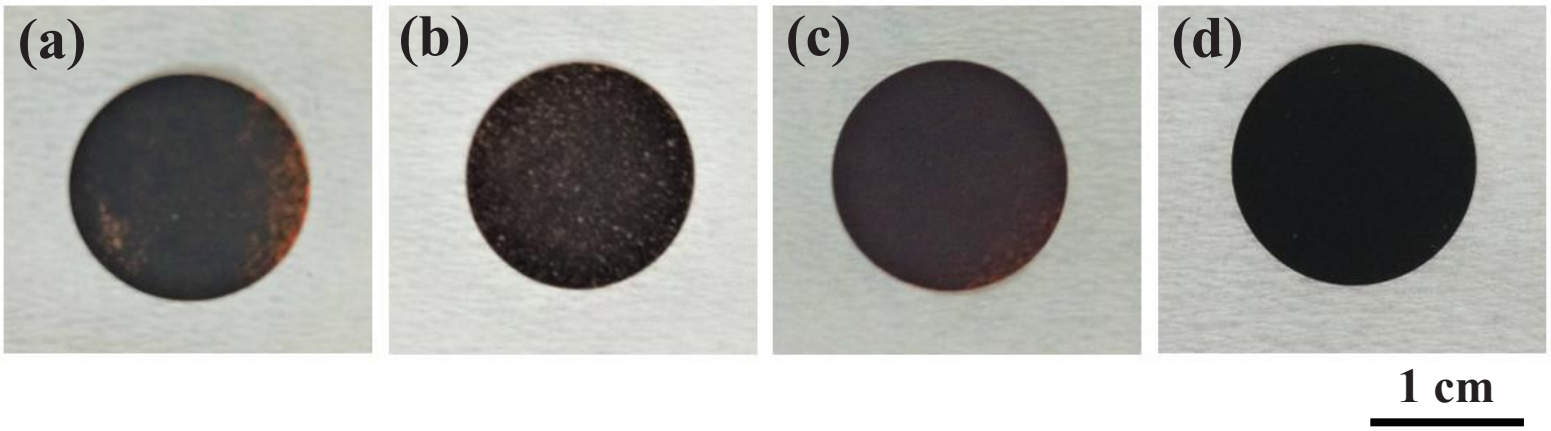


**Figure S11.** Surface appearances of (a) PVDF, (b) NaCMC, (c) NaPAA, and (d) NaCMC/NaPAA electrodes after 300 charge–discharge cycles.

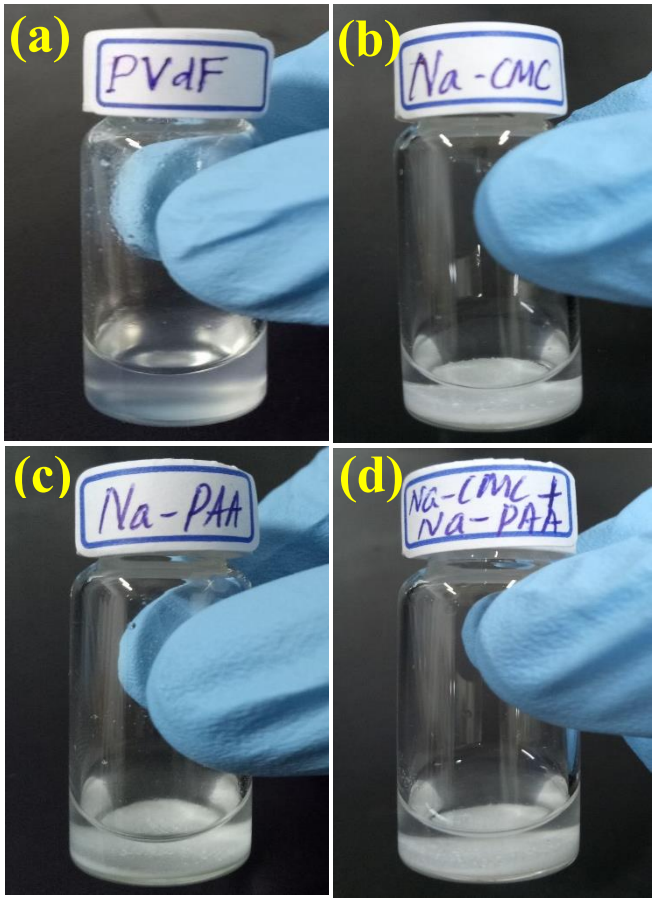


**Figure S12.** Photographs of (a) PVDF, (b) NaCMC, (c) NaPAA, and (d) NaCMC/NaPAA binders immersed in 1 M $NaClO_4$ PC/EC/FEC electrolyte.